The role of fibril structure and surface hydrophobicity in secondary nucleation of amyloid fibrils

Dev Thacker[a] , Kalyani Sanagavarapu[a], Birgitta Frohm[a], Georg Meisl[b] , Tuomas P. J. Knowles[b,c], and Sara Linse[a,1]

[a]Department of Biochemistry and Structural Biology, Lund University, SE22100 Lund, Sweden; [b]Department of Chemistry, University of Cambridge, Cambridge CB2 1EW, United Kingdom; and [c]Cavendish Laboratory, University of Cambridge, Cambridge CB3 0HE, United Kingdom

Crystals, nanoparticles, and fibrils catalyze the generation of new aggregates on their surface from the same type of monomeric building blocks as the parent assemblies. This secondary nucleation process can be many orders of magnitude faster than primary nucleation. In the case of amyloid fibrils associated with Alzheimer's disease, this process leads to the multiplication and propagation of aggregates, whereby short-lived oligomeric intermediates cause neurotoxicity. Understanding the catalytic activity is a fundamental goal in elucidating the molecular mechanisms of Alzheimer's and associated diseases. Here we explore the role of fibril structure and hydrophobicity by asking whether the V18, A21, V40, and A42 side chains which are exposed on the Aβ42 fibril surface as continuous hydrophobic patches play a role in secondary nucleation. Single, double, and quadruple serine substitutions were made. Kinetic analyses of aggregation data at multiple monomer concentrations reveal that all seven mutants retain the dominance of secondary nucleation as the main mechanism of fibril proliferation. This finding highlights the generality of secondary nucleation and its independence of the detailed molecular structure. Cryo-electron micrographs reveal that the V18S substitution causes fibrils to adopt a distinct morphology with longer twist distance than variants lacking this substitution. Self- and cross-seeding data show that surface catalysis is only efficient between peptides of identical morphology, indicating a templating role of secondary nucleation with structural conversion at the fibril surface. Our findings thus provide clear evidence that the propagation of amyloid fibril strains is possible even in systems dominated by secondary nucleation rather than fragmentation.

amyloid | strain propagation | surface catalysis | secondary nucleation

The amyloid β peptide (Aβ) has been identified through genetic and histological studies to be involved in the pathology of Alzheimer's disease (AD) (1–3) with characteristic extracellular deposits in which the peptide is assembled into amyloid fibrils and plaques. The peptide exists as multiple length variants, and the 42-residue peptide Aβ42 is one of the most aggregation-prone alloforms (4). In its native form, Aβ42 is monomeric and unstructured. However, during the pathology of AD, Aβ42 undergoes self-assembly and forms highly ordered amyloid aggregates through a series of microscopic steps. Specifically, this self-assembly process involves primary nucleation, secondary nucleation, and elongation (5). Primary nucleation involves monomers only, whereas secondary nucleation involves both monomer and an already existing aggregate, formed from the same type of monomers. Fibrils thus provide a catalytic surface which enhances the rate of nucleation (Fig. 1 A and B) (5). Secondary nucleation initially leads to the formation of oligomers, which can subsequently convert to mature fibrils. Oligomers are considered to be the neurotoxic species in the pathology of AD (6–8). However, the exact mechanism of nucleation and oligomer formation by the interaction of Aβ42 monomers with the fibril surface remains challenging to characterize.

Several structures of Aβ42 fibrils have been reported, based on cryogenic electron microscopy and solid-state NMR (ssNMR) data, hinting at a strong influence of the sample conditions on the observed structures (9–11). Fibrils found in strongly acidic

samples in high content of organic solvent are very different from those found at physiological pH (10). For Aβ40 there is very large variation between reported structures. A highly interesting study in this respect used brain-derived samples, dominated by Aβ40, revealing considerable polymorphism, presumably caused by the coexistence of multiple length variants in a complex environment (11). The current in vitro study relies on simplified systems of homogeneous peptides in buffer at physiological pH. Such conditions have led to the reproducible observation of the same Aβ42 fibril structure through three totally independent efforts in terms of sample preparation and ssNMR investigation (12–14). It is expected that pure samples adopt identical structures under the same solution conditions, and these reproducible structures thus provide a resource for experimental design toward the understanding of structural and molecular determinants of secondary nucleation around physiological pH. Of particular interest is the fibril surface and these structures reveal that residues 1 to 14 are in the relatively disordered N-terminal part, while the side chains of K16, V18, A21, E22, D23, S26, K28, V40, and A42 are more or less exposed on the surface of the ordered part of the fibril. In particular, four hydrophobic side chains are found on the surface of the fibril core: Val18, Ala21, Val40, and Ala42 (Fig. 1C) (12, 13).

These four residues are distributed as two hydrophobic patches on the fibril surface; Val18 and Ala21 comprise one hydrophobic patch, and Val40 and Ala42 form the other one. These arrangements are found twice in every cross-section of the filament, each cross-section comprising two monomers, such that

Significance

Alzheimer's disease affects a rapidly growing number of individuals worldwide. Key unresolved questions relate to the onset and propagation of the disease, linked to the self-assembly of amyloid β peptide into fibrillar and smaller aggregates. This study investigates the propagation of aggregates of amyloid β peptide and asks whether hydrophobic molecular features observed on the fibril surface correlate with its ability to catalyze the formation of new aggregates. This question is motivated by the associated formation of intermediate forms that are toxic to neuronal cells. The results imply that surface catalysis is independent of surface details but requires that the monomers that form the new aggregate can adopt the structure of the parent aggregate without steric clashes.

Fig. 1. The solid-state NMR structure of Aβ42 and the microscopic steps involved in its self-assembly. Primary nucleation (*A*) involves the formation of nuclei from monomers alone (spheres), while in secondary nucleation (*B*) the fibrils (rectangles) act as a catalytic surface (seeds) for the formation of new aggregates. Oligomers are the product of both nucleation events. (*C*) Solid-state NMR structure showing the Aβ42 fibril core. The exposed hydrophobic residues which are addressed in this study are shown in red, and other hydrophobic residues which are buried toward the inside are shown in yellow. The exposed hydrophobic residues form two separate patches. V18 and A21 form a hydrophobic patch in a groove. V40 and A42 form a hydrophobic patch which is highly exposed. (*D*) List of peptides involved in this study along with their amino acid sequences.

Val40 and Ala42 form two continuous hydrophobic strips on each filament and Val18 and Ala21 are located in two hydrophobic grooves on each filament. For the surface-enhanced nucleation of Aβ42 monomers (substrate) on Aβ42 fibrils (catalysts) one might expect that the hydrophobic patches on the fibril are involved in substrate binding as well as product formation (catalysis), in particular since secondary nucleation has been associated with a low energy barrier of entropic nature (15).

In this work, we thus ask whether the four hydrophobic residues V18, A21, V40, A42 and the patches they form are involved in the interaction with Aβ42 monomers during the process of secondary nucleation, linked to oligomer formation. We have generated seven mutants in which hydrophobic residues are replaced with serine, a hydrophilic amino acid. We designed four single mutants, V18S, A21S, V40S, and A42S, in order to test the effect of each of these residues on secondary nucleation, two double mutants for the two hydrophobic patches, (18+21)S and (40+42)S, and a quadruple mutant (4S) in which all four of these hydrophobic residues have been replaced with serine (Fig. 1*C*). To understand the effect of these serine mutations and the influence of hydrophobic residues on secondary nucleation, we studied the concentration and time-dependent aggregation kinetics of all seven mutants using thioflavin T (ThT) fluorescence. We performed self-seeding of each mutant as well as cross-seeding of each mutant versus wild type (WT) Aβ42 to find out whether WT seeds catalyze the aggregation of mutant monomers and vice versa. In

addition, we used cryogenic transmission electron microscopy (cryo-TEM) and ANS (8-anilinonaphthalene-1-sulfonic acid) fluorescence to study the effect of the hydrophobic residue substitutions on fibril morphology and surface properties.

Results

Expression and Purification of Hydrophobic Patch Mutants. Kinetic analysis of protein aggregation and its mechanistic analysis is enabled by advances in experimental approaches that have allowed highly reproducible aggregation kinetics to be recorded. It is increasingly apparent that the sequence purity of the starting material is crucial for this approach. We thus expressed recombinantly WT human Aβ42 as is, that is, without any tags except Met0, which is required to initiate translation, and purified from inclusion bodies using ion exchange and size-exclusion steps, essentially as described (16, 17). This mode of expression of Aβ(M1-42) peptides requires that the peptide has low enough solubility to form inclusion bodies, which avoids the degradation of small unstructured proteins in *Escherichia coli*. We attempted expression as is for all single, double, and quadruple mutants, which was found feasible for A21S, V40S, A42S, and (40+42)S, which are thus used in the form of Aβ(M1-42) peptides. V18S, (18+21)S, and 4S gave very low yield and were instead expressed in fusion with the self-cleavable tag NPro in the form of its EDDIE mutant, which drives the expressed fusion construct to inclusion bodies and cleaves off the fused peptide upon refolding. These mutants are thus used in the form of Aβ1-42 peptides. As a reference we produced and purified the WT both in the form of Aβ(M1-42) and Aβ1-42. If not otherwise specified, WT Aβ42 refers to WT Aβ(M1-42).

Aggregation Kinetics. The fibril formation of the peptides with serine replacing hydrophobic side chains was investigated under conditions at which Aβ42 is known to aggregate rapidly (5, 18). Aggregation starting from freshly purified monomers at 1.1 to 10 μM was thus followed by monitoring ThT fluorescence as a function of time and peptide concentration at 37 °C in 20 mM sodium phosphate and 0.2 mM ethylenediaminetetraacetic acid (EDTA), pH 8.0, for WT Aβ42 and all seven mutants. Under these conditions, all seven serine mutant peptides form ThT-positive aggregates over time. All aggregation curves have a sigmoidal-like appearance, comprising a lag phase, an exponential phase, and a final plateau, characteristic of nucleated polymerization reactions (see Fig. 3). All nucleation and growth processes are active during all three phases, and a steady state is reached during the plateau phase (19). We observe that for all for all mutants the lag phase is extended and the overall aggregation retarded compared to WT Aβ42.

The time at which half the monomer is converted to fibril, $t_{1/2}$, versus the initial monomer concentration is shown in Fig. 2 with logarithmic axes. We find that all mutants show retarded aggregation compared to the WT peptide over the entire concentration range. The mutant with aggregation behavior most similar to the WT peptide is A21S, with a half-time $t_{1/2}$ of 0.61 h at 10 μM initial monomer and a concentration dependence similar to WT, while the 4S peptide aggregates most slowly with a $t_{1/2}$ of 4.33 h at 10 μM, compared to 0.20 h for the WT peptide and with a flatter concentration dependence (Fig. 2). Interestingly, the scaling exponent, which describes the dependence of $t_{1/2}$ on the peptide concentration, is similar between the A21S mutant (−1.15) and WT peptide (−1.24), an observation which suggests that the aggregation is likely to be governed by a similar mechanism (5, 19). The scaling exponents for the other of the mutants range from −0.37 to −0.77, which may indicate a shift in the aggregation mechanism, or increased saturation of secondary nucleation (discussed below).

Kinetic Analysis. The aggregation data for each mutant were analyzed by global fitting of rate laws to the experimental data

using the AmyloFit platform (17). This analysis allows us to connect macroscopic measurements of protein aggregation to the fundamental microscopic events, including nucleation and growth processes, which underlie the overall aggregation phenomenon, and to determine the microscopic rate constants of these processes. Through this approach, we can compare different peptide systems based on their molecular mechanism of aggregation. To this effect, models of varying complexity were tested and we find that none of the data for the mutants can be fitted using models lacking secondary nucleation (*SI Appendix*, Fig. S1), whereas all data are well fitted by a model including secondary nucleation of monomers on the fibril surface (Fig. 3). This observation implies that secondary nucleation, which dominates the aggregation mechanism of the WT peptide, is retained as the key process by which new aggregates are formed for all mutants of the current study. Examples of aggregation data and the best fit using a model which includes multistep secondary nucleation are shown in Fig. 3. This model describes an aggregation mechanism that consists of three microscopic steps, primary nucleation (rate constant k_n), elongation (k_+), and surface-catalyzed secondary nucleation (k_2), and allows the catalytic surface for secondary nucleation to saturate, similar to the Michaelis–Menten model for enzyme kinetics (20, 21). The kinetic analysis of unseeded aggregation experiments yields two effective kinetic parameters which are products of the microscopic rate constants, k_+k_n and k_+k_2, referred to as the combined rate constants for the primary and secondary pathways, respectively, and a parameter, $\sqrt{K_M}$, describing the monomer concentration at half saturation of the secondary nucleation process (the reaction orders of the nucleation steps were assumed to be the same as in the WT). The measured aggregation kinetics initiated from the monomer state depend only on these products, not the rate constants individually (22).

Readily interpretable quantities, which can be used to compare systems at different degrees of saturation, are the rates at which new fibril mass is formed through the pathways involving primary or secondary nucleation, denoted by λ and κ, respectively (see *Materials and Methods* for detailed definitions). These quantities, evaluated at a reference monomer concentration of 3 μM, are shown in Fig. 4 *A* and *B*, respectively. For all mutants κ is at least an order of magnitude higher than λ. This observation provides strong evidence that surface-catalyzed secondary nucleation is the dominant mechanism for the generation of new fibrils, even upon removal of the hydrophobic residues from the Aβ42 fibril surface.

We find that for all mutants κ is decreased somewhat compared to the WT, by up to an order of magnitude. By contrast,

primary processes appear to be less systematically affected; λ remains unchanged for most mutants and is significantly affected only for V18S and the quadruple mutant, for which it is decreased by 3 orders of magnitude. In addition to the rates, we have also evaluated the saturation concentration of secondary nucleation, $\sqrt{K_M}$, which is shown in Fig. 4*C*. Only the WT and all mutants involving the A21S substitution show appreciable saturation over the range of monomer concentrations sampled, with A21S being the least saturated. All other mutants are fully saturated even at the lowest concentrations used. This indicates that all mutations other than A21S lead to increased affinity of the monomers for the fibril surface.

Morphology of Aggregates. Cryo-TEM was used to study the morphology of the end-stage fibrils for all mutants and WT Aβ42. In typical WT Aβ(M1-42) aggregates, individual filaments can be observed, and two filaments are twisted around each other along a common axis, seen as nodes that appear along the fibril at regular intervals (Fig. 5). The fibrils are short and rigid and cluster together on the sample grid, indicating highly hydrophobic behavior. Fibrils of the Aβ (1-42) peptide were also imaged as a control and show very similar morphology and node-to-node distances in the same range as for Aβ(M1-42) WT (*SI Appendix*, Fig. S7). Fibrils of the mutant A21S show morphology most similar to the WT Aβ42 fibrils. The filaments seem to twist sharply around each other and the intervals between the nodes is short. Similar features are found for V40S and A42S and the double mutant (40+42)S. However, the fibrils of the V18S mutant seem to have a quite different morphology compared to the WT peptide. The twist has a longer pitch, that is, the distance between the nodes is noticeably longer (Fig. 5). The fibrils also appear to be longer and more flexible than the WT Aβ42 fibrils and moreover do not clump together on the sample grid but seem to be more evenly spread. The fibrils of the double mutant (18+21)S also seem to have a structure very similar to the V18S fibrils, which indicates that replacement of Val18 with serine causes the fibril morphology to change. Also, the 4S mutant formed fibrils which were starkly different from the WT fibrils but similar to the V18S mutant, which once again indicates that the V18S substitution causes an alteration of the fibril morphology. Fig. 6 shows the distribution of the node-to-node distances among the fibrils of the mutant peptides, measured assuming all fibrils are orthogonal to the incident beam, and as such are minimum distances. The V18S mutant shows the largest separation between nodes (∼92 to 144 nm) and the other mutants in which the Val18 has been replaced also show large node-to-node distances [4S ∼63 to 87 nm, (18+21)S ∼68 to 99 nm]. The fibrils of the remaining mutants have shorter distances between the nodes, which are more comparable to the fibrils of the WT Aβ42.

For most of the peptides we detected very little polymorphism, but in some instances there was a coexistence of ∼2 to 4% of straight fibrils with 96 to 98% of twisted fibrils.

Self-Seeding and Cross-Seeding Aggregation Experiments. Self-seeding and cross-seeding studies of each mutant with WT Aβ42 were performed in order to probe whether the WT seeds catalyze nucleation of the mutant monomers and vice versa. The results are detailed below and summarized in Fig. 7. Self-seeding experiments were set up for each mutant by adding preformed seeds to freshly purified monomers of the same mutant. Cross-seeding experiments were set up for each mutant by adding preformed seeds of WT Aβ42 to freshly purified monomers of the mutant, and in converse by adding preformed seeds of mutant Aβ42 to freshly purified monomers of the WT Aβ42. Seed concentrations ranged from 0 to 30% of the monomer concentration in monomer units. The normalized ThT fluorescence curves of the seeded aggregation kinetics are shown in *SI Appendix*, Fig. S2. The lag phase decreases as the seed concentration increases in cases of self-seeding and in cross-seeding
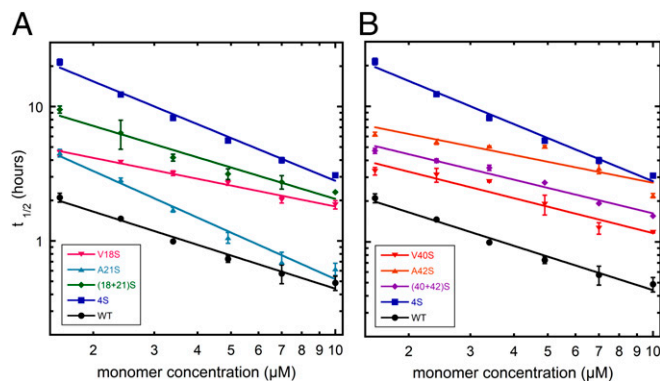
Fig. 2. The time of half completion, $t_{1/2}$, is plotted on logarithmic scale as a function of peptide concentration for the serine mutants in comparison with the WT Aβ42 in 20 mM sodium phosphate and 200 μM EDTA at pH 8.0. Error bars represent the SD of three replicates as shown in Fig. 3, and the data from the three replicates are averaged. (*A*) The mutants of the (18+21) hydrophobic patch are shown in comparison with the quadruple mutant peptide and the WT peptide, and (*B*) compares the mutants of the (40+42) hydrophobic patch.
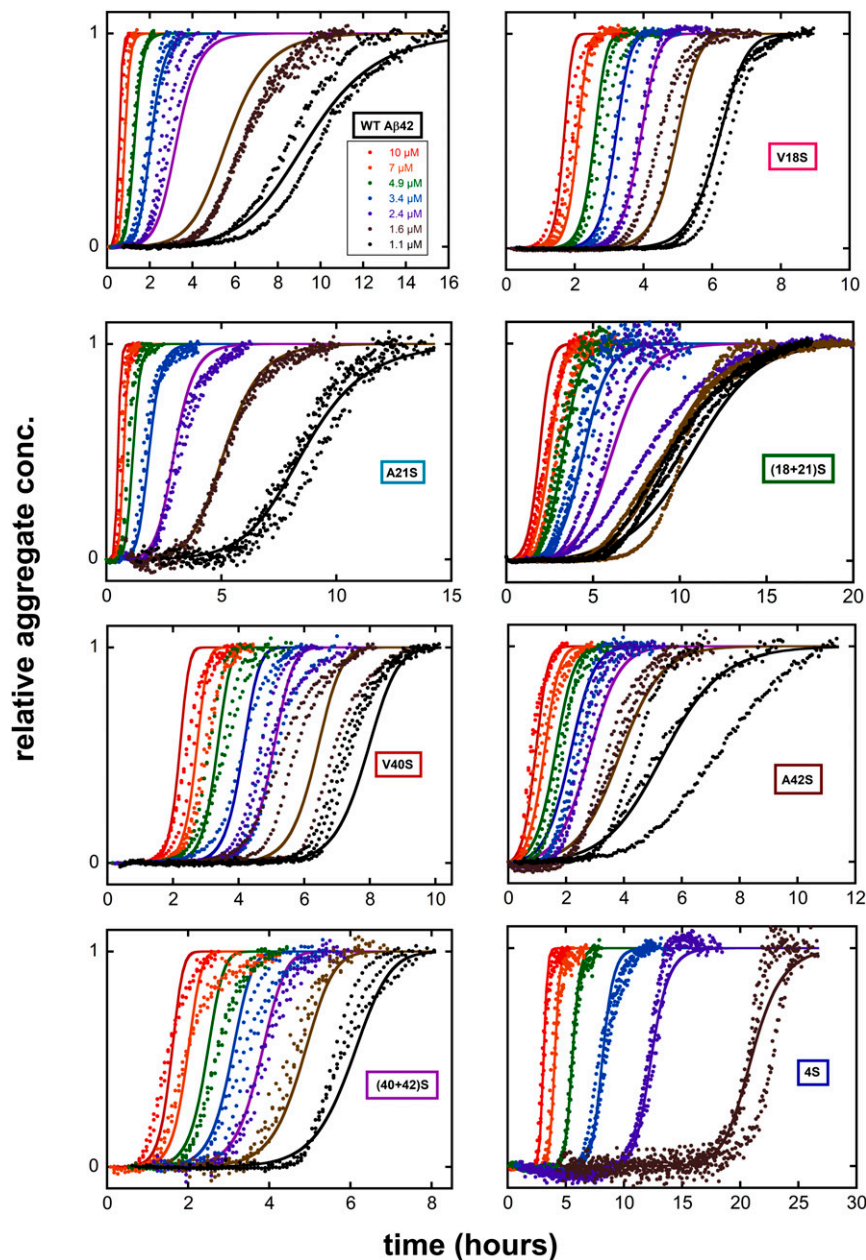
Fig. 3. Aggregation kinetics for WT Aβ42 and seven serine mutant peptides as monitored by ThT fluorescence are shown. Aggregation was monitored in the presence of 6 μM ThT in 20 mM sodium phosphate and 200 μM EDTA at pH 8.0 for 1.1, 1.6, 2.4, 3.4, 4.9, 7, and 10 μM of each peptide (color codes given in the top left panel are the same for all of the peptides). Data are from a single experiment with three replicates for each concentration. The global fitting to all data for each peptide done using AmyloFit is shown with the curves at each concentration in the same color as the respective data points. The best fit was obtained using the multistep secondary nucleation dominant model for all of the peptides. The aggregation data for 1.1 μM concentration of the 4S mutant are not shown because achieving reproducible aggregation kinetics at lower concentrations proved to be difficult.

conditions if cross-catalysis is effective. The half-time plots for the cross-seeding experiments are shown in Fig. 8 *C–F*.

Substitution of the 40/42 hydrophobic patch does not seem to hinder cross-seeding. In the case of the V40S mutant, there is a strong self-seeding effect. With respect to cross-seeding, the aggregation of V40S monomers is catalyzed equally well by WT seeds and V40S seeds, whereas WT monomer is catalyzed better by WT seeds than by V40S seeds. The WT monomer is catalyzed strongly by seeds of the A42S mutant, whereas the aggregation of the A42S monomer is catalyzed better by WT seeds than by A42S seeds. The double mutant, (40+42)S, displays very similar self-seeding and cross-seeding effects for both WT and the mutant monomers. These findings indicate that substitution of hydrophobic

residues at positions 40 and 42 does not affect surface nucleation, as the WT monomer is catalyzed equally well by the mutant and WT seeds, and vice versa. Fig. 8*D* shows the concentration dependence of the surface catalysis of WT monomers on the seeds of the 40+42 hydrophobic patch mutants.

Substitution of the 18/21 hydrophobic groove interferes with seeding. The A21S mutant monomer shows a more pronounced cross-seeding effect than self-seeding, and the aggregation of the WT monomer is catalyzed better by WT seeds than A21S seeds. However, the WT monomers are not seeded by V18S mutant seeds, and the V18S monomers are much better self-seeded than cross-seeded with WT seed. The aggregation of V18S monomer is accelerated only when supplemented by 30% WT seeds, but at
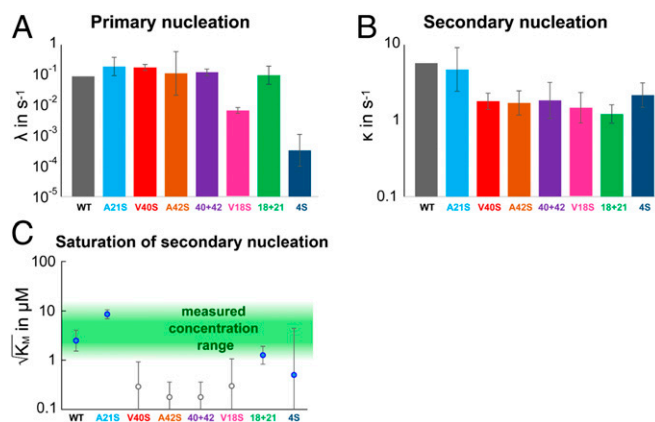
Fig. 4. Results of the global fitting of data for each mutant. Error bars are SDs over replicates and repeats of the experiment. (*A*) Rates at which new fibril mass is being produced through the pathways involving primary nucleation, evaluated at a representative monomer concentration of 3 μM. (*B*) Rates at which new fibril mass is being produced through the pathways involving secondary nucleation, evaluated at a representative monomer concentration of 3 μM. (*C*) The monomer concentration at half saturation of secondary nucleation.

lower seed concentrations no seeding effect is observed. This indicates that replacing the Val18 with serine renders the mutant monomer unable to nucleate on WT seeds, and vice versa. This effect persists in the case of the double mutant (18+21)S as well, for which self-seeding is prominent, and cross-seeding does not occur. The quadruple mutant, 4S, is catalyzed strongly by its own seeds but less by WT seeds, in which case a prominent lag phase is noticed even at high seed concentrations. Moreover, the aggregation of 4S monomers is not seeded by Aβ (1-42) seeds. Neither Aβ(M1-42) nor Aβ (1-42) WT monomers are seeded by 4S fibrils (Fig. 8*A* and *SI Appendix*, Fig. S2). These observations make clear that upon substitution of the Val18 residue the WT monomer fails to seed on the mutant fibrils. Fig. 8*C* shows the inability of Val18 mutants to catalyze the nucleation of WT monomers and hence the flatter concentration dependence as compared to the WT self-seeding.

We also investigated a few cases of mutant–mutant cross-seeding. The V18S monomers are better seeded by fibrils of the double mutant (18+21)S than by fibrils of WT Aβ42. Conversely, the aggregation of monomers of (18+21)S is better seeded by V18S fibrils than by WT fibrils (Fig. 9 and *SI Appendix*, Fig. S3*A*). Cross-seeding studies between mutants reveal that V18S fibrils fail to catalyze the aggregation of both V40S and (40+42)S monomers. Conversely, V18S monomers are not seeded by fibrils of V40S, although they are catalyzed by (40+42)S fibrils (Fig. 9 and *SI Appendix*, Fig. S3 *D* and *E*).

Aβ40 fibrils display a long node-to-node distance (Fig. 6) (23). It has been previously found that Aβ40 does not nucleate on the surface of Aβ42 fibrils and vice versa (23), but here we find that Aβ40 WT monomers are prominently seeded when supplemented with the fibrils of the V18S mutant (*SI Appendix*, Fig. S3*B*). Monomers of the 4S mutant show approximately similar seeding effect from Aβ40 and Aβ42 fibrils, but the aggregation from monomers of Aβ40 is not catalyzed by fibrils of the 4S mutant in the range 0.3 to 10% (*SI Appendix*, Fig. S4*A*). Mutant–mutant cross-seeding studies show that monomers of A21S, V40S, and (40+42)S all show either weak or no seeding effect in the presence of 4S seeds and, conversely, 4S monomers show weak to no seeding effect on the fibrils of A21S, V40S, and (40+42)S peptides (Fig. 9 and *SI Appendix*, Fig. S4 *B–D*).

ANS Fluorescence. ANS is used as a fluorescent molecular probe that when excited at 350 nm gives a weak fluorescence maximum at 530 nm in water but upon binding to hydrophobic surfaces of proteins gives a fluorescence maximum around 490 nm (24). ANS fluorescence was thus measured to estimate the

surface hydrophobicity of the WT and mutant Aβ42 fibrils. ANS was titrated against 5 μM fibrils of each individual peptide, starting from 5 μM ANS up to ~70 to 100 μM ANS, when a plateau in the fluorescence was achieved. Fig. 10 shows the fluorescence intensity at 490 nm as a function of ANS concentration for fibrils of each variant. It is well known that WT Aβ42 fibrils are hydrophobic, and as expected significant ANS fluorescence was observed in the presence of WT Aβ42 fibrils (Fig. 10 and *SI Appendix*, Fig. S8). The hydrophobic substitutions did not alter the blue shift of the fluorescence maximum to any large extent and lead to at most a 50% reduction in the ANS fluorescence intensity. Thus, even in the case of the 4S mutant, relatively high ANS fluorescence intensity was observed and a similar ANS concentration is needed to reach saturation of the mutant and WT (Fig. 10). The consistently high ANS fluorescence indicates that upon substitution of the hydrophobic residues on the Aβ42 fibril surface the peptide folds in a way that exposes other hydrophobic residues on the fibril surface.

Discussion

The aggregation mechanism of Aβ42 has been resolved in the past decade in terms of its underlying microscopic steps: primary nucleation, elongation, and secondary nucleation. In secondary nucleation, Aβ42 fibrils provide a catalytic surface for nucleation, amplifying the production of new fibrils as well as oligomeric intermediates. A connection between the fibril surface properties and secondary nucleation is thus expected. The four hydrophobic residues that are exposed on the surface of the Aβ42 fibril core (Val18, Ala21, Val40, and Ala42) can be grouped into two hydrophobic patches, Val18+Ala21 and Val40+Ala42 (12, 13). This arrangement is intriguing in light of the many systems (enzymes, interfacial catalysts, and beyond) where hydrophobic grooves, clefts, or surfaces have been inferred to affect catalysis either through enhanced substrate binding or through modulation of the catalytic activity (25–33). However, higher affinity does not always govern catalysis; the Sabatier principle states that there is an optimal substrate affinity above which reduced product release impedes catalysis and below which catalysis is reduced due to insufficient substrate binding (34). Indeed, the same phenomenon is predicted for secondary nucleation already in minimal models of fibril formation (35).

The comparison of self- and cross-seeding data has been used in several cases over the last decades to understand the sequence determinants of seed-catalyzed nucleation and elongation, for example of the prion protein (36). In this study, we set out to investigate the role hydrophobic residues in surface-catalyzed secondary nucleation of Aβ42. Through the design of four single mutants, V18S, A21S, V40S, and A42S, we assessed the individual effect of these residues on secondary nucleation as well as cross-nucleation of WT. In addition, we investigated two double mutants targeting the two hydrophobic patches, (18+21)S and (40+42)S, and a quadruple mutant in which all four of these hydrophobic residues have been replaced with serine.

We performed unseeded as well as self-seeded aggregation kinetics for each of the single mutants, double mutants, and the quadruple mutant to study the position-dependent role of hydrophobic residues on secondary nucleation. We find that the same aggregation mechanism as for WT Aβ42, albeit with saturation of secondary nucleation, can be used to globally fit the experimental data for all of the serine mutants. The A21S mutant is most similar to the WT Aβ42 and its secondary nucleation step is the least saturated. By contrast, V18S aggregates more slowly and its secondary nucleation is fully saturated. The double mutant, (18+21)S, appears to display an additive effect in terms of overall retardation and secondary nucleation saturates at a monomer concentration between that of A21S and V18S. The single substitutions at the [40+42] hydrophobic patch also cause longer lag phase and larger $t_{1/2}$ compared to the WT peptide, with A42S slower than V40S. The double mutant (40+42)S aggregates at an intermediate rate and the secondary nucleation
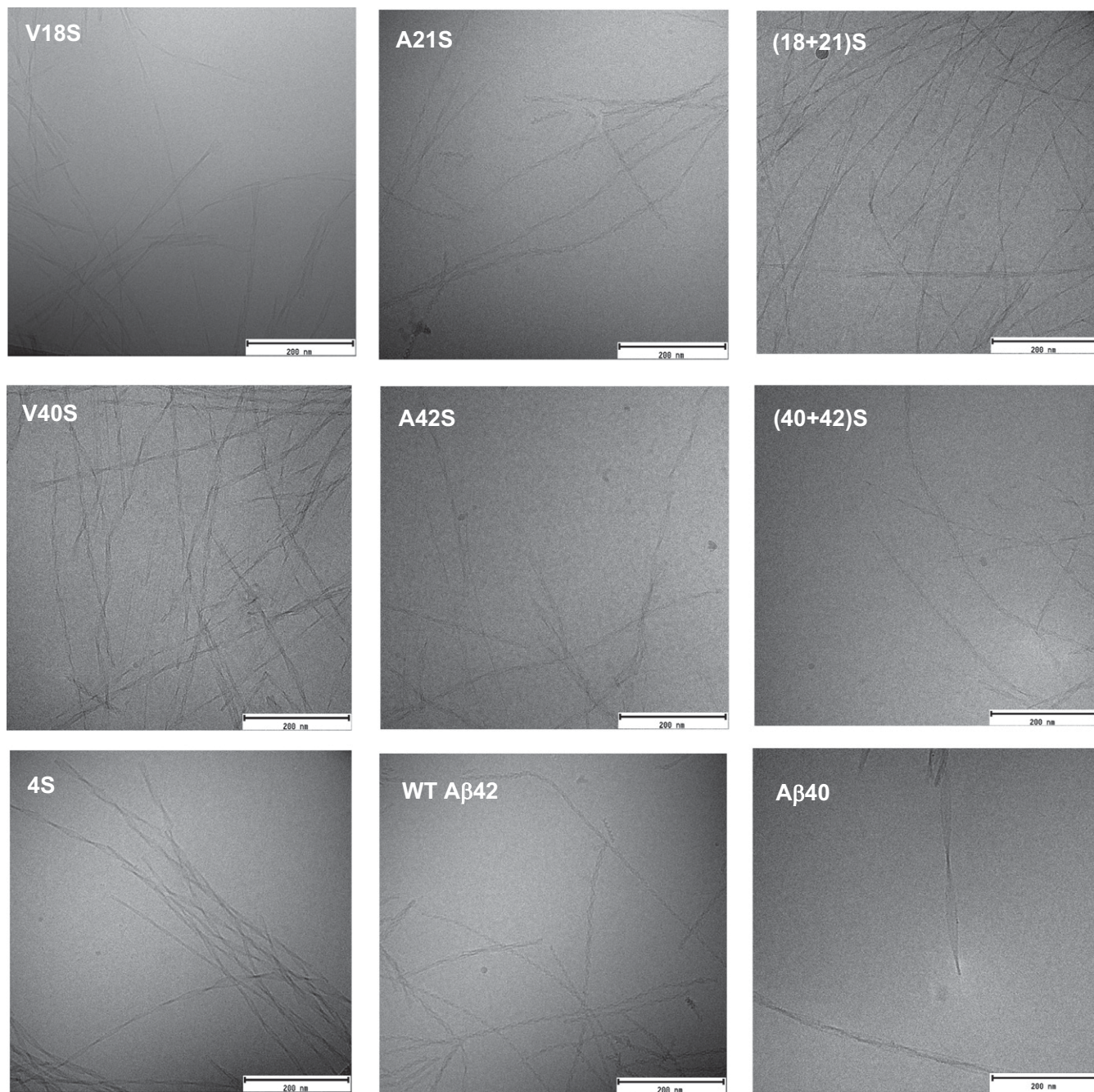
Fig. 5. Cryo-TEM of end-stage fibrils of the serine mutants V18S, A21S, (18+21)S, V40S, A42S, (40+42)S and 4S, WT Aβ42, and Aβ40. A typical WT Aβ42 fibril shows the presence of two filaments twisted around each other in a way that creates nodes at regular intervals along the fibril. Fibrils formed by some of the mutants show different morphologies than the WT peptide in terms of the node-to-node distance.

step of all three mutants is fully saturated. The lowest rate of aggregation is found for 4S and is almost exclusively due to a reduction in the rate constant for primary nucleation by ∼3 orders of magnitude. Most likely this is an effect of reduced hydrophobicity of the mutant peptide, making primary nucleation less favorable.

For all mutants we find that the rate of secondary nucleation is somewhat decreased but broadly in the same range as that for WT Aβ42. Thus, all mutants retain the dominance of secondary nucleation for the generation of new aggregates. Remarkably, this finding implies that none of the four hydrophobic residues that are exposed on the Aβ42 fibril surface is necessary for secondary nucleation to take place. Either this means that

removal of the hydrophobic patches does not hinder the secondary nucleation or the mutants are folded in a different way exposing new hydrophobic residues, as discussed further below. In any case, it is clear that up to four hydrophobic residues can be replaced by serine in the Aβ42 sequence while still retaining secondary nucleation. This finding goes well in hand with the observations that secondary nucleation is a prominent process for a range of self-assembling systems, including biopolymers and small molecules (37, 38), and even the simplest possible spherical structures, Lennard-Jones particles (39). Thus, no particular structure may be required for secondary nucleation to be effective.

While all serine mutant proteins form highly ordered fibrils, the cryo-TEM images reveal that some of the mutant fibrils
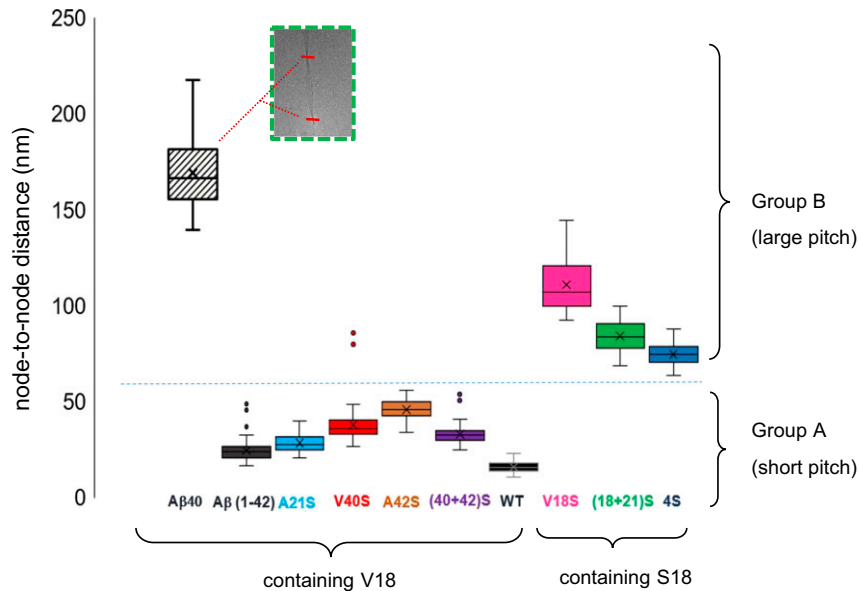
Fig. 6. Analysis of the fibril morphology based on the cryo-TEM images (Fig. 5) in terms of the node-to-node distance distributions. Node-to-node distance for a fibril can be defined as the distance between two consecutive nodes created by the twisting of the two filaments of a fibril on top of each other at regular intervals (*Inset*). This analysis shows that the serine mutants can be classified into two separate groups. Group A are the mutants that show shorter distance between two nodes and sharper twists and have fibril morphology that is similar to WT Aβ42. The mutants that have different morphology than the fibrils of WT Aβ42 can be classified under group B. These are the mutant peptides which have longer node-to-node distance in the fibrils. All of the mutants falling in group B contain the V18S substitution. Data for Aβ (1-42) is shown as control. For each peptide, ∼100 node-to-node distances were measured, with approximately six to seven measurements per fibril, from ∼35 different areas of the cryo-TEM sample grid. In the plot, the box contains the middle 50% data points, the line indicates the median, and the whiskers include all data points.

possess a morphology that is distinctly different from that of WT Aβ42 fibrils. Analysis of the fibril morphology shows that the mutants can be clearly demarcated into two separate groups based on the distance between consecutive nodes in the fibrils for all of the serine mutant peptides (Fig. 6). All of the peptides containing the V18S mutation have much longer distances between two nodes of their fibrils and can be classified as group B. The remaining mutants have shorter node-to-node distances and can be classified into a separate group, A. All mutants display a significant blue shift and relatively high ANS fluorescence despite the replacement of hydrophobic residues with serine. The most extreme example is the 4S mutant, which in principle should have no hydrophobic residues exposed on the surface of the fibril core if it were folded in the same way as the WT peptide fibril. The blue shift and relatively high ANS fluorescence thus points toward an altered fibril core.

For three of the group A mutant peptides, V40S, A42S, and (40+42)S, we cannot detect any changes in morphology relative to WT, and we can conclude that replacing the 40/42 hydrophobic strip with hydrophilic side chains does not abolish secondary nucleation. Moreover, these three peptides display surface nucleation on WT fibrils, and WT monomers nucleate effectively on the fibrils of these variants. In other words, these peptides could be classified as forming fibrils of the same strain as WT Aβ42.

The combined cryo-TEM and ANS data suggest that group B mutant peptides are folded in a different way in the fibrils, thereby exposing another set of hydrophobic residues at an altered fibril surface. Our cross-seeding experiments reveal that this renders the group B fibrils incompatible to act as seeds to catalyze nucleation of WT Aβ42. All of the group B mutants [V18S, (18+21)S, and 4S] fail to cross-seed with WT. Thus, WT Aβ42 fails to nucleate on the surface of group B fibrils. Conversely, the group B mutant monomers do not nucleate on the WT Aβ42 fibrils. Some of the mutant peptides, including 4S, were recombinantly produced as Aβ1-42 using EDDIE fusion and autoproteolysis (*Materials and Methods*),

because their high solubility prevents expression "as is" in *E. coli*. The cross-seeding of 4S was therefore separately investigated with Aβ1-42 WT (Fig. 8) and Aβ(M1-42) WT (*SI Appendix*, Fig. S2); these have been inferred to have the same fibril core structure but some detectable interactions between the N terminus and core in Aβ(M1-42) fibrils are not observed for Aβ1-42 (40). We find that both Aβ142 and Aβ(M1-42) WT monomers fail to nucleate on 4S seeds. The 4S monomers fail to nucleate on Aβ1-42 WT seeds but show weak cross-seeding by Aβ(M1-42) but still much weaker than the self-seeding.

Fig. 7. Summary of all seeding experiments. Tick marks indicate all cases for which seeding occurs and a cross for those in which it does not. Yellow circles indicate that a cross-seeding effect was observed but not as prominent as self-seeding. The green boxes indicate that the two peptides fall into the same group based on the morphology of their fibrils. The pink boxes indicate that the two peptides fall into different groups based on the morphology of their fibrils.
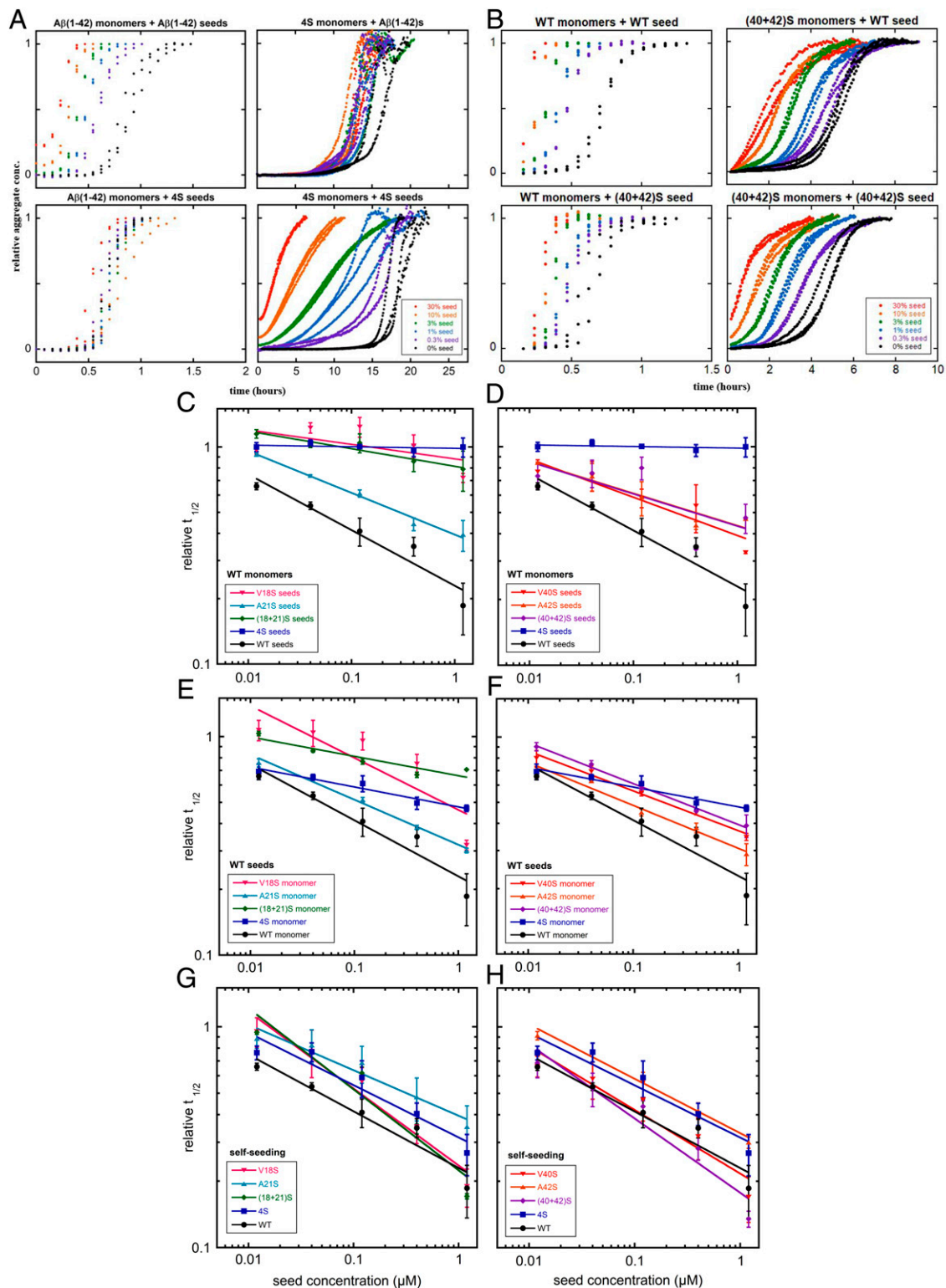
Fig. 8. Self- and cross- seeding studies. (*A*) The self-seeding of Aβ (1-42) and its cross-seeding with the 4S mutant is shown, as well as the self-seeding of 4S mutant and its cross-seeding with Aβ (1-42). (*B*) The self-seeding of WT Aβ42 and its cross-seeding with the (40+42)S double mutant is shown, as well as the self-seeding of the (40+42)S mutant and its cross-seeding with WT Aβ42. (*C–F*) The half-time of completion, $t_{1/2}$, for self- and cross-experiments of WT Aβ42 and each of the seven serine mutants is plotted on logarithmic scale as a function of seed concentration. All experiments are performed in 20 mM sodium phosphate and 200 μM EDTA at pH 8.0. Error bars represent the SD of three replicates as shown in *SI Appendix*, Fig. S2, and the data from the three replicates are averaged. (*C*) The cross-seeding of WT Aβ42 monomers on the seeds of the mutants of the (18+21) hydrophobic patch is shown in comparison with the quadruple mutant seeds and Aβ42 self-seeding, and (*D*) compares the cross-seeding of WT Aβ42 monomers on the seeds of the mutants of the (40+42) hydrophobic patch with that of the quadruple mutant seeds and the self-seeding of WT Aβ42. (*E*) The cross-seeding of the monomers of the mutants of the (18+21) hydrophobic patch on the seeds of WT Aβ42 is shown in comparison with that of the quadruple mutant monomers and the self-seeding of WT Aβ42, and (*F*) shows the cross-seeding of the monomers of the mutants of the (40+42) hydrophobic patch on the seeds of WT Aβ42. (*G* and *H*) Show the self-seeding of the mutants of the (18+21) and (40+42) hydrophobic patches, respectively.
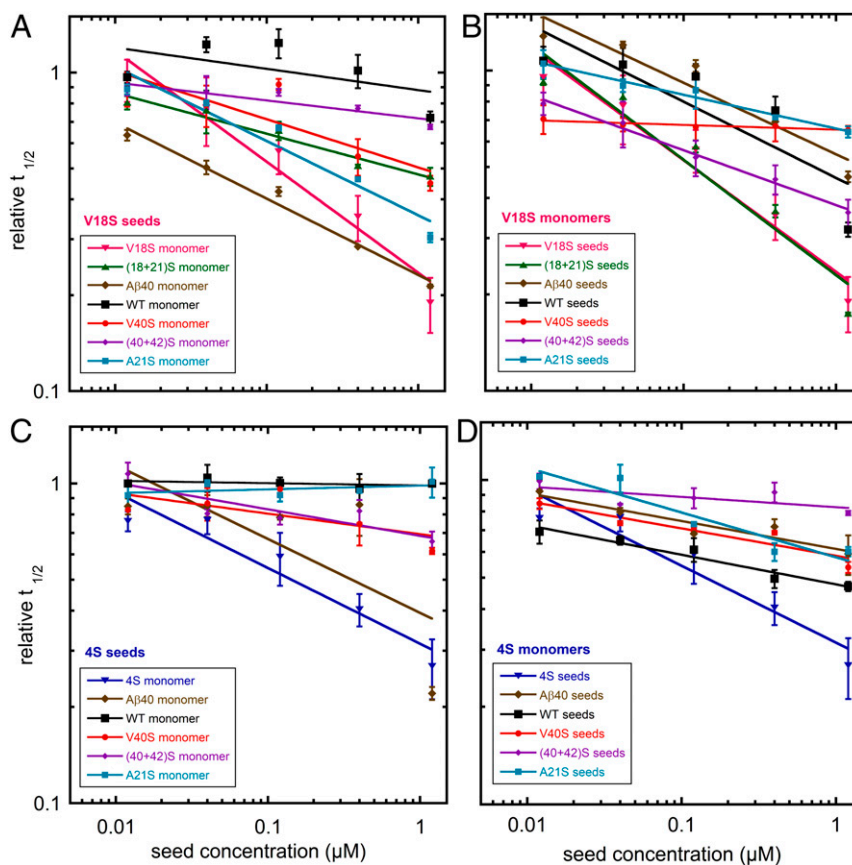
Fig. 9. Seeding experiments between Group A and Group B mutants. The half-time of completion, $t_{1/2}$, is plotted on logarithmic scale as a function of seed concentration for A21S, (18+21)S, V40S, (40+42)S, Aβ40, and WT Aβ42 monomers in presence of V18S seeds in comparison with the self-seeding of V18S (*A*). (*B*) The cross-seeding of V18S monomers with A21S, (18+21)S, V40S, (40+42)S, Aβ40, and WT Aβ42. Cross-seeding of monomers of A21S, V40S, (40+42)S, Aβ40, and WT Aβ42 in presence of 4S seeds is shown in comparison with the self-seeding of 4S. (*C* and *D*) The cross-seeding of 4S monomers with A21S, V40S, (40+42)S, Aβ40, and WT Aβ42. Error bars represent the SD of three replicates as shown in *SI Appendix*, Figs. S3 and S4, and the data from the three replicates are averaged. Experiments were performed in the presence of 6 µM ThT in 20 mM sodium phosphate and 200 µM EDTA at pH 8.0. For seeding experiments involving Aβ40, the monomer concentration was 10 µM at pH 7.4 in the presence of 20 µM ThT.

The change in the morphology and core structure caused by the V18S mutation thus hinders surface catalyzed nucleation of peptides lacking this substitution. This is a very strong indication that the ability of monomers to nucleate on a fibril surface is linked to the ability of the monomers to adopt the parent structure and implies a templating role of secondary nucleation.

The A21S peptide falls in group A in terms of fibril morphology, but this variant displays some features suggesting that it may indeed form a group of its own. This peptide is unique among the variants in that self-seeding seems less effective than cross-seeding with WT.

To provide further evidence that the structure and morphology of the fibril is an important factor in surface-catalyzed secondary nucleation, we performed cross-seeding of V18S and (18+21)S, which both fall in group B. The results show that V18S nucleates much faster on (18+21)S fibrils than on the WT fibrils. Conversely, the seeding of (18+21)S monomers by V18S fibrils, although not as strong as the self-seeding, is still better than the seeding by WT Aβ42 fibrils. Again, the presence of V18 or S18 appears to be a structural switch that disables surface cross-catalysis.

Finally, another variant of the Aβ peptide that is believed to be of importance in AD is Aβ40, two residues shorter than Aβ42. It has been shown that Aβ40 does not nucleate on the surface of Aβ42 fibrils, and vice versa. Analysis of the fibril morphology of Aβ40 has also revealed longer node-to-node distances compared to Aβ42 fibrils (23) (Fig. 6). Thus, Aβ40 also falls in the same morphology group (B) as the mutants containing the V18S substitution. To further investigate

the effect of fibril morphology on surface-catalyzed nucleation, we therefore performed cross-seeding experiments for the V18S mutant against WT Aβ40. Indeed, when provided with V18S seed fibrils, the aggregation of Aβ40 is efficiently catalyzed. The aggregation of V18S monomers is similarly seeded by fibrils of Aβ40 and Aβ42 WT. This supports that for surface catalyzed secondary nucleation to occur the monomer must be able to adopt the structure of the parent fibril.

It is well known that amyloid fibrils can be propagated in vitro and in vivo (41–43). The concept of strain is commonly used to refer to a distinct morphology that is propagated by additional monomers forming aggregates of the same morphology. Numerous studies have employed heavy seeding conditions to propagate distinct strains, which is usually proposed to occur through elongation and fragmentation, which is kinetically favored over nucleation under such conditions. This makes it possible for the monomers added to the fibril ends to adopt the same structure as the monomers in the seed fibril even if this is not the thermodynamically most stable form under the conditions used (44). Such procedures have enabled structural investigations of brain polymorphs through seeding with isotope-enriched monomers that propagate the disease-associated strain (45, 46). While fragmentation is an obvious way for fibrils to multiply and propagate morphology, it has been proposed that amyloid structure can be propagated through secondary nucleation (47) in a similar manner as seen in many other systems (37, 38). The perceived difficulty of propagating strain information through surface-catalyzed
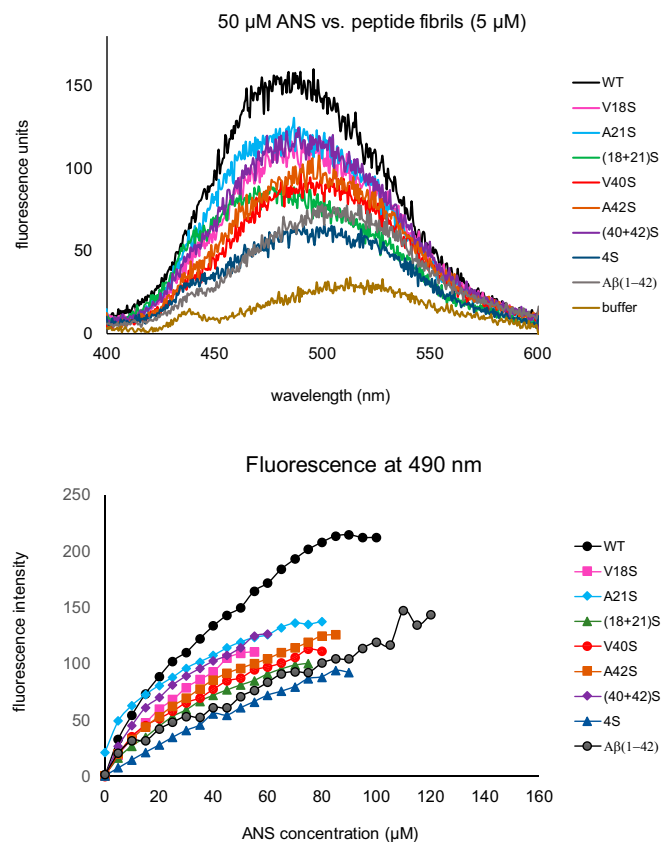
Fig. 10. ANS fluorescence. All of the seven serine mutants and WT Aβ42 were titrated with ANS to examine the surface hydrophobicity. (*A*) Representative spectra at 50 μM ANS and (*B*) the titration curves of V18S (pink), A21S (cyan), (18+21)S (green), V40S (red), A42S (brown), (40+42)S (violet), 4S (blue), and WT Aβ42 (black). ANS was titrated into 5 μM of preformed peptide fibrils in steps of 5 μM until saturation was achieved. ANS shows high fluorescence upon binding to WT Aβ42. WT Aβ42 also saturates at the highest concentration of ANS (90 μM). The 4S mutant fibrils show high ANS fluorescence as well, and are saturated by ANS concentrations comparable to that for the WT fibrils (80 μM), implying that upon removing the hydrophobic residues exposed on the fibril surface the fibril might be folding in a different way, causing other buried hydrophobic residues to be exposed on the surface. The ANS titration data for Aβ (1-42) is shown as control. All spectra are shown in *SI Appendix*, Fig. S8.

nucleation, rather than fragmentation, has shed doubts on the relevance of secondary nucleation in situations where strain propagation occurs. However, our results clearly show that surface nucleation can be highly selective, being altered by a single mutation, and its effectiveness correlates well with morphological features of the formed fibrils.

While the current investigation is focused on the molecular determinants of nucleation on the fibril surface, our self- and cross-seeding data cover also the high-seed regime. We can thus conclude that the ability of monomers to cross-elongate fibril seeds follows the same trend as cross-nucleation. The A21S, V40S, A42S, and (40+42)S variants are fully compatible with elongation of WT seeds, and vice versa, whereas all variants containing the V18S substitution lack this property. Clearly, the V18S substation serves as a structural switch hindering both elongation and surface nucleation between the group A and group B variants.

Conclusion

In conclusion, the results of the present work very clearly show that none of the four residues V18, A21, V40, and A42 is required for secondary nucleation of monomers on a fibril surface to take place. However, our results also show that all variants that contain the V18S substitution have an altered fibrillar structure and that the ability of

monomers to nucleate on a fibril surface is very strongly linked to the ability of the monomers to take up the parent structure. Remarkably, the node-to-node distance measured by cryo-TEM, as a proxy for fibril structure, was a good predictor of this ability to cross-seed, as verified by additional seeding experiments with Aβ40. Thus, the removal of hydrophobic residues fundamentally alters the sequence requirements for seeding propagation of the parent structure, while maintaining the overall rate of this process at approximately the same level. These findings highlight that secondary nucleation is at the same time highly specific in propagating the parent structure, while also being a general feature whose presence is robust toward sequence and structural perturbations.

Materials and Methods

Expression and Purification of Peptides. The plasmids carrying synthetic genes with *E. coli* optimized codons for Aβ42 WT [PetSac, cloned by us (16)] as well as A21S, V40S, A42S, and (40+42)S (Pet3a, purchased from Genscript) were transformed into Ca²⁺-competent cells of *E. coli* strain BL21 DE3 pLysS star and the proteins were expressed in autoinduction medium (48). The peptides were purified using ion exchange chromatography (IEX) as described (16) with the minor change that a lower salt concentration (50 mM NaCl) was used to elute the peptides, and size-exclusion chromatography (SEC) on a 26- × 600-mm Superdex 75 column was used instead of spin filters for molecular mass fractionation. The purified monomeric peptides were lyophilized as aliquots until further use.

Expression and Purification of EDDIE-Tagged Constructs. V18S, (18+21)S, and 4xS were expressed using a fusion construct with the self-cleavable tag EDDIE (13). The plasmids carrying synthetic genes with *E. coli* optimized codons for EDDIE-Aβ42 V18S as well as (18+21)S and 4xS (Pet3a, purchased from Genscript) were transformed into Ca²⁺-competent cells of *E. coli* strain BL21 DE3 pLysS star and the proteins were expressed in autoinduction medium (48). The cell pellet from 1.5 L culture was sonicated five times in 10 mM Tris·HCl and 1 mM EDTA, pH 8.5, with a trace of DNase, 50 mL each time. After each sonication, the lysate was centrifuged for 7 min at 15,000 rpm (5,534.1 × *g*) and the supernatant removed. The inclusion body pelleted after the fifth sonication was dissolved in 70 mL 10 M urea, 10 mM Tris, 1 mM EDTA, and 1 mM dithiothreitol (DTT), pH 8.5, by sonication and stirring. When dissolved, the urea solution was diluted with 80 mL 10 mM Tris, 1 mM EDTA, and 1 mM DTT, pH 8.5, and loaded onto 3- × 5-mL DEAE-FF columns in tandem. Before this, the column was preequilibrated in 10 mM Tris, 1 mM EDTA, and 1 mM DTT, pH 8.5, with 4 M urea. The column was washed with 100 mL 4 M urea, 10 mM Tris, 1 mM EDTA, and 1 mM DTT, pH 8.5, and eluted with a linear gradient from 0 to 0.4 M NaCl in 4 M urea, 10 mM Tris, 1 mM EDTA, and 1 mM DTT, pH 8.5 (180-mL gradient). The fractions were collected using a fraction collector, analyzed by sodium dodecyl sulfate polyacrylamide gel electrophoresis (SDS/PAGE), and pooled together into one or more pools depending on their purity. Each pool was diluted 15 times with 10 mM Tris, 1 mM EDTA, and 5 mM DTT, pH 8.5, in a glass bottle, placed in a cold room, and left there for 48 to 72 h to cleave off the EDDIE tag. Cleavage was monitored using SDS/PAGE. The Aβ42 mutants were then purified from EDDIE using IEX in batch format on Q-Sepharose big beads and eluted with 50 mM NaCl, lyophilized, dissolved in 6 M GuHCl, 20 mM sodium phosphate, and 0.2 mM EDTA, pH 8.5, and further purified using SEC on 26 × 600 mm Superdex 75 column. The monomer was lyophilized as aliquots until further use.

Preparation of Samples for Kinetic Experiments. The lyophilized aliquots of the purified peptides were dissolved in 1 mL of 6 M GuHCl, 20 mM sodium phosphate, and 0.2 mM EDTA, pH 8.5, and subjected to gel filtration on a Superdex 75 10/300 column in 20 mM sodium phosphate buffer, pH 8.0, with 0.2 mM EDTA. The middle part of monomer peak was collected in a low-binding tube (Axygen) on ice and was typically found to have a concentration in the range 20 to 80 μM (determined by absorbance of the collected part of the chromatogram peak using $\varepsilon_{280} = 1,400$ L mol⁻¹·cm⁻¹). The collected monomer was supplemented with 6 μM ThT from a 2.7 mM stock, and dilutions were performed as explained below.

Aggregation Kinetics by ThT Fluorescence. Aggregation kinetics experiments were performed as a function of peptide concentration. The highest concentration of the peptide was 10 μM, and the solution was logarithmically diluted with the buffer to final concentrations ranging down to 1.1 μM into a 96-well plate (Corning 3881), 100 μL per well using a tailor-made pipetting robot (49). The experiments were initiated by placing the 96-well plate at 37 °C in a plate reader (Fluostar Omega). The ThT fluorescence was measured through the bottom of the plate every 120 s. The excitation filter was at 440 nm, and the emission filter was at 480 nm.

Self-seeding and cross-seeding experiments were performed with a monomer concentration of 4 μM. Seed concentrations were 30, 10, 3, 1, 0.3, and 0% in monomer equivalents. A monomer stock solution of 8 μM concentration was prepared in a low-binding tube. Seeds were prepared from a starting monomer concentration of 10 μM in a 96-well plate. These were then diluted to 2× the final required concentrations. 50 μL of the desired seeds were added from the respective 2× stock solutions, and then 50 μL of the monomer solution was added to each well from the stock, giving a total of 100 μL of 1× seeds + 1× monomers in each well. All dilutions were performed in 20 mM sodium phosphate buffer, pH 8.0, with 0.2 mM EDTA and 6 μM ThT.

Aβ40 aggregates much slower compared to Aβ42 and requires a higher monomer concentration (20). As such, the seeding experiments involving Aβ40 were performed with a monomer concentration of 10 μM at pH 7.4 and 20 μM ThT for Aβ40, and 4 μM at pH 8.0 and 6 μM ThT for the mutant peptide. For Aβ40, seeds were prepared from a starting monomer concentration of 20 μM in a 96-well plate. The pH of these seeds was adjusted to 8.0 before adding to the mutant monomers, and the pH of the mutant seeds was adjusted to 7.4 before adding to Aβ40 monomers.

Analysis of Aggregation Kinetics. The analysis of the aggregation kinetics to determine the molecular mechanism and the rate constants underpinning this process was performed using the fitting platform AmyloFit (17). The kinetic data were uploaded, normalized and fitted using the online AmyloFit interface. This analysis uses equations derived by considering the contributions from primary nucleation, secondary nucleation, and elongation. The model multistep secondary nucleation dominated was successful in fitting all experimental data. In this model the fraction of aggregated proteins at time t is given by

$$\frac{[M]_t}{[M]_\infty} = 1 - \left(1 - \frac{[M]_0}{[M]_\infty}\right)e^{-k_\infty t}\left(\frac{B_- + C_+ e^{\kappa t}}{B_+ + C_+ e^{\kappa t}}\frac{B_+ + C_+}{B_- + C_+}\right)^{\frac{\kappa^2}{\kappa\beta}},$$

where the definitions of the parameters are

$$\kappa = \sqrt{2[m]_0 k_+ \frac{[m]_0^{n_2} k_2}{1 + [m]_0^{n_2}/K_M}}$$

$$\lambda = \sqrt{2k_+ k_n [m]_0^{n_c}}$$

$$C_\pm = \frac{k_+[P]_0}{\kappa} \pm \frac{k_+[M]_0}{2[m]_0 k_+} \pm \frac{\lambda^2}{2\kappa^2}$$

$$\alpha = 2k_+[P]_\infty$$

$$\beta = \sqrt{\alpha^2 - 4C_+ C_- \kappa^2}$$

$$B_\pm = \frac{\alpha \pm \beta}{2\kappa}$$

and where $[m]_0$ is the initial monomer concentration; $[P]_0$, $[M]_0$, and $[P]_\infty$,

$[M]_\infty$ are the aggregate number and mass concentration at the beginning and end of aggregation, respectively (see ref. 17 for detailed expression of $[P]_\infty$); k_+, k_n, and k_2 are the rate constants of elongation, primary and secondary nucleation, respectively; and n_c and n_2 are the reaction orders of primary and secondary nucleation, respectively.

Cryo-TEM. For all peptides, samples of 10 μM monomer were incubated at 37 °C in PEGylated plates (Corning 3881) in a plate reader and collected after reaching the plateau in ThT fluorescence. For Aβ40 the sample concentration was 20 μM at pH 7.4, which was then diluted to 10 μM and pH changed to 8.0 before sample preparation. Specimens for cryo-TEM were prepared in an automatic plunge freezer system (Leica EM GP). The climate chamber temperature was kept at 21 °C, and relative humidity was ≥90% to minimize loss of solution during sample preparation. The specimens were prepared by placing 4 μL solution on glow-discharged lacey formvar carbon-coated copper grids (Ted Pella) and blotted with filter paper before being plunged into liquid ethane at −183 °C. This leads to vitrified specimens, avoiding component segmentation and rearrangement, and the formation of water crystals, thereby preserving original microstructures. The vitrified specimens were stored under liquid nitrogen until measured. A Fischione Model 2550 cryo transfer tomography holder was used to transfer the specimen into the electron microscope, JEM 2200FS, equipped with an in-column energy filter (Omega filter), which allows zero-loss imaging. The acceleration voltage was 200 kV and zero-loss images were recorded digitally with a TVIPS F416 camera using SerialEM under low-dose conditions with a 10-eV energy selecting slit in place.

ANS Binding Assay. ANS was titrated against 5 μM peptide (WT Aβ42 or each of the mutants) and fluorescence emission spectra were measured using a PerkinElmer LS50B luminescence spectrometer and a QS quartz cuvette of 10-mm path length. The ANS was diluted from a 10 mM stock to a series of concentrations starting from 10 μM up to the point at which saturation of fluorescence was achieved (∼70 to 100 μM, varying according to the peptide titrated against). The excitation wavelength was 380 nm and the emission range was from 400 nm to 600 nm. The excitation slit width was 5 nm and the emission slit width was 10 nm.

1. S. G. Younkin, The role of A β 42 in Alzheimer's disease. *J. Physiol. Paris* **92**, 289–292 (1998).
2. R. E. Tanzi, L. Bertram, Twenty years of the Alzheimer's disease amyloid hypothesis: A genetic perspective. *Cell* **120**, 545–555 (2005).
3. Y. S. Eisele *et al.*, Peripherally applied Abeta-containing inoculates induce cerebral beta-amyloidosis. *Science* **330**, 980–982 (2010).
4. O. Szczepankiewicz *et al.*, N-terminal extensions retard Aβ42 Fibril Formation but allow cross-seeding and coaggregation with Aβ42. *J. Am. Chem. Soc.* **137**, 14673–14685 (2015).
5. S. I. A. Cohen *et al.*, Proliferation of amyloid-β42 aggregates occurs through a secondary nucleation mechanism. *Proc. Natl. Acad. Sci. U.S.A.* **110**, 9758–9763 (2013).
6. M. Bucciantini *et al.*, Inherent toxicity of aggregates implies a common mechanism for protein misfolding diseases. *Nature* **416**, 507–511 (2002).
7. D. M. Walsh *et al.*, Naturally secreted oligomers of amyloid beta protein potently inhibit hippocampal long-term potentiation in vivo. *Nature* **416**, 535–539 (2002).
8. C. Haass, D. J. Selkoe, Soluble protein oligomers in neurodegeneration: Lessons from the Alzheimer's amyloid beta-peptide. *Nat. Rev. Mol. Cell Biol.* **8**, 101–112 (2007).
9. M. Schmidt *et al.*, Peptide dimer structure in an Aβ(1-42) fibril visualized with cryo-EM. *Proc. Natl. Acad. Sci. U.S.A.* **112**, 11858–11863 (2015).
10. L. Gremer *et al.*, Fibril structure of amyloid-β(1-42) by cryo-electron microscopy. *Science* **358**, 116–119 (2017).
11. M. Kollmer *et al.*, Cryo-EM structure and polymorphism of Aβ amyloid fibrils purified from Alzheimer's brain tissue. *Nat. Commun.* **10**, 4760 (2019).
12. M. T. Colvin *et al.*, Atomic resolution structure of monomorphic Aβ42 amyloid fibrils. *J. Am. Chem. Soc.* **138**, 9663–9674 (2016).
13. M. A. Wälti *et al.*, Atomic-resolution structure of a disease-relevant Aβ(1-42) amyloid fibril. *Proc. Natl. Acad. Sci. U.S.A.* **113**, E4976–E4984 (2016).
14. Y. Xiao *et al.*, Aβ(1-42) fibril structure illuminates self-recognition and replication of amyloid in Alzheimer's disease. *Nat. Struct. Mol. Biol.* **22**, 499–505 (2015).
15. S. I. A. Cohen *et al.*, Distinct thermodynamic signatures of oligomer generation in the aggregation of the amyloid-β peptide. *Nat. Chem.* **10**, 523–531 (2018).
16. D. M. Walsh *et al.*, A facile method for expression and purification of the Alzheimer's disease-associated amyloid beta-peptide. *FEBS J.* **276**, 1266–1281 (2009).
17. G. Meisl *et al.*, Molecular mechanisms of protein aggregation from global fitting of kinetic models. *Nat. Protoc.* **11**, 252–272 (2016).
18. E. Hellstrand, B. Boland, D. M. Walsh, S. Linse, Amyloid β-protein aggregation produces highly reproducible kinetic data and occurs by a two-phase process. *ACS Chem. Neurosci.* **1**, 13–18 (2010).
19. P. Arosio, T. P. J. Knowles, S. Linse, On the lag phase in amyloid fibril formation. *Phys. Chem. Chem. Phys.* **17**, 7606–7618 (2015).
20. G. Meisl *et al.*, Differences in nucleation behavior underlie the contrasting aggregation kinetics of the Aβ40 and Aβ42 peptides. *Proc. Natl. Acad. Sci. U.S.A.* **111**, 9384–9389 (2014).
21. A. J. Dear *et al.*, The catalytic nature of protein aggregation. *J. Chem. Phys.* **152**, 045101 (2020).
22. S. I. A. Cohen *et al.*, Nucleated polymerization with secondary pathways. I. Time evolution of the principal moments. *J. Chem. Phys.* **135**, 065105 (2011).
23. R. Cukalevski *et al.*, The Aβ40 and Aβ42 peptides self-assemble into separate homo-molecular fibrils in binary mixtures but cross-react during primary nucleation. *Chem. Sci.* **6**, 4215–4233 (2015).

24. A. Málnási-Csizmadia, G. Hegyi, F. Tölgyesi, A. G. Szent-Györgyi, L. Nyitray, Fluorescence measurements detect changes in scallop myosin regulatory domain. *Eur. J. Biochem.* **261**, 452–458 (1999).

25. T. A. Steitz, R. Henderson, D. M. Blow, Structure of crystalline alpha-chymotrypsin. 3. Crystallographic studies of substrates and inhibitors bound to the active site of alpha-chymotrypsin. *J. Mol. Biol.* **46**, 337–348 (1969).

26. C. S. Wang, Probing of active site structure of lipoprotein lipase: Contribution of activation entropy in the catalysis. *Biochim. Biophys. Acta* **1212**, 67–72 (1994).

27. Y. S. Kulkarni *et al.*, Enzyme architecture: Modeling the operation of a hydrophobic clamp in catalysis by triosephosphate isomerase. *J. Am. Chem. Soc.* **139**, 10514–10525 (2017).

28. Y. Jeong *et al.*, Solubilization of hydrophobic catalysts using nanoparticle hosts. *Small Weinh. Bergstr. Ger.* **14**, 1702198 (2018).

29. S. L. Chong *et al.*, Immobilization of bacterial feruloyl esterase on mesoporous silica particles and enhancement of synthetic activity by hydrophobic-modified surface. *Bioresour. Technol.* **293**, 122009 (2019).

30. B. Feng *et al.*, Hydrophobic catalysis and a potential biological role of DNA unstacking induced by environment effects. *Proc. Natl. Acad. Sci. U.S.A.* **116**, 17169–17174 (2019).

31. Z. Qin *et al.*, Improving galactooligosaccharide synthesis efficiency of β-Galactosidase Bgal1-3 by reshaping the active site with an intelligent hydrophobic amino acid scanning. *J. Agric. Food Chem.* **67**, 11158–11166 (2019).

32. B. Greydanus, D. K. Schwartz, J. W. Medlin, Controlling catalyst-phase selectivity in complex mixtures with amphiphilic janus particles. *ACS Appl. Mater. Interfaces* **12**, 2338–2345 (2020).

33. R. Fernandez-Lafuente, P. Armisén, P. Sabuquillo, G. Fernández-Lorente, J. M. Guisán, Immobilization of lipases by selective adsorption on hydrophobic supports. *Chem. Phys. Lipids* **93**, 185–197 (1998).

34. E. Roduner, Understanding catalysis. *Chem. Soc. Rev.* **43**, 8226–8239 (2014).

35. A. Šarić *et al.*, Physical determinants of the self-replication of protein fibrils. *Nat. Phys.* **12**, 874–880 (2016).

36. J. H. Come, P. E. Fraser, P. T. Lansbury Jr., A kinetic model for amyloid formation in the prion diseases: Importance of seeding. *Proc. Natl. Acad. Sci. U.S.A.* **90**, 5959–5963 (1993).

37. G. D. Botsaris, "Secondary nucleation—A review" in *Industrial Crystallization*, J. W. Mullin, Ed. (Springer, 1976), pp. 3–22.

38. S. G. Agrawal, A. H. J. Paterson, Secondary nucleation: Mechanisms and models. *Chem. Eng. Commun.* **202**, 698–706 (2015).

39. J. Anwar, S. Khan, L. Lindfors, Secondary crystal nucleation: Nuclei breeding factory uncovered. *Angew. Chem. Int. Ed. Engl.* **54**, 14681–14684 (2015).

40. R. Silvers *et al.*, Aggregation and fibril structure of $A\beta_{M01-42}$ and $A\beta_{1-42}$. *Biochemistry* **56**, 4850–4859 (2017).

41. J. T. Jarrett, P. T. Lansbury Jr., Seeding "one-dimensional crystallization" of amyloid: A pathogenic mechanism in Alzheimer's disease and scrapie? *Cell* **73**, 1055–1058 (1993).

42. M. Jucker, L. C. Walker, Self-propagation of pathogenic protein aggregates in neurodegenerative diseases. *Nature* **501**, 45–51 (2013).

43. Z. Jaunmuktane *et al.*, Evidence for human transmission of amyloid-β pathology and cerebral amyloid angiopathy. *Nature* **525**, 247–250 (2015).

44. A. Peduzzo, S. Linse, A. K. Buell, The properties of α-synuclein secondary nuclei are dominated by the solution conditions rather than the seed fibril strain. *ACS Chem. Neurosci.* **11**, 909–918 (2020).

45. A. K. Paravastu, I. Qahwash, R. D. Leapman, S. C. Meredith, R. Tycko, Seeded growth of β-amyloid fibrils from Alzheimer's brain-derived fibrils produces a distinct fibril structure. *Proc. Natl. Acad. Sci. U.S.A.* **106**, 7443–7448 (2009).

46. W. Qiang, W.-M. Yau, J.-X. Lu, J. Collinge, R. Tycko, Structural variation in amyloid-β fibrils from Alzheimer's disease clinical subtypes. *Nature* **541**, 217–221 (2017).

47. L. E. Orgel, Prion replication and secondary nucleation. *Chem. Biol.* **3**, 413–414 (1996).

48. F. W. Studier, Protein production by auto-induction in high density shaking cultures. *Protein Expr. Purif.* **41**, 207–234 (2005).

49. R. Frankel *et al.*, Autocatalytic amplification of Alzheimer-associated Aβ42 peptide aggregation in human cerebrospinal fluid. *Commun. Biol.* **2**, 365 (2019).

BIOPHYSICS AND COMPUTATIONAL BIOLOGY